ACS Catalysis

RESEARCH ARTICLE

pubs.acs.org/acscatalysis

Pt–Ru Alloyed Fuel Cell Catalysts Sputtered from a Single Alloyed Target

Arrelaine A. Dameron,*[†] Tim S. Olson,[†] Steven T. Christensen,[†] Jennifer E. Leisch,[†] Katherine E. Hurst,[†] Svitlana Pylypenko,[†,‡] Justin B. Bult,[†] David S. Ginley,[†] Ryan P. O'Hayre,[‡] Huyen N. Dinh,[†] and Thomas Gennett[†]

[†]National Renewable Energy Laboratory, 1617 Cole Blvd., Golden, Colorado 80401, United States

[‡]Colorado School of Mines, 1500 Illinois St., Golden, Colorado 80401, United States

ABSTRACT: This work illustrates the improved performance of a direct menthol fuel cell (DMFC) $Pt_{1-x}Ru_x$ alloy phase catalysts deposited via magnetron sputtering onto a carbon powder matrix from an alloyed mixed-metal target. The production of dispersed metal catalysts particles of the correct size, structure, bulk, and surface composition for effective methanol oxidation required extensive control of process parameters including sputter gas type, sputter gas concentration, deposition pressure, sputter power, and sputter type (RF or DC). Through the adjustment of these multivariate sputtering parameters, it was possible to make alloyed catalyst materials with varying crystallinity and composition ranging from $Pt_{0.32}Ru_{0.68}$ to $Pt_{0.50}Ru_{0.50}$. The careful balance of these parameters resulted in a low metal loading catalyst, ~30 wt %, with a methanol oxidation reaction onset potential of <300 mV versus RHE and peak current of >200 uA/cm^2. The optimized sputtered catalysts have increased metal utilization and outperform commercially available catalysts at fuel cell operating potentials.

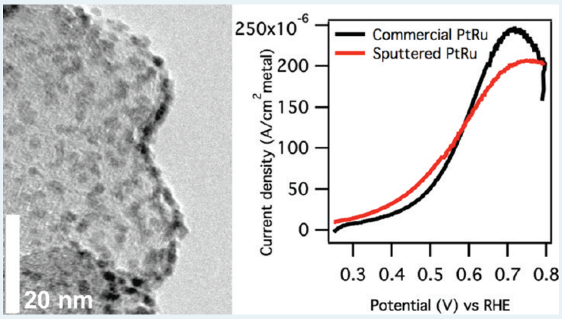

KEYWORDS: platinum, ruthenium, alloy, DC sputtering, RF sputtering, cosputtering, direct methanol fuel cells

INTRODUCTION

Direct methanol fuel cells (DMFCs) have the potential to provide high operating efficiency in an environmentally friendly package for portable power applications. The high energy density and ease of storage of the liquid fuel makes DMFCs readily applicable.[1,2] While pure Pt catalysts are not ideal for use as anode catalysts in this system, Pt-alloy materials serve as bifunctional catalysts to reduce the poisoning of Pt by carbon monoxide, (CO), a byproduct of methanol oxidation.[3] Of particular interest is the $Pt_{1-x}Ru_x$ alloy system, which has proven to increase performance by several enhancement mechanisms.[1,4−6] Important to the lifetime of the Pt-based catalysts is the role of ruthenium to provide hydroxyl-like species to oxidize CO to CO_2, which in turn reduces CO poisoning of the catalyst.[1]

In current state-of-the-art DMFCs, high precious metal loadings are required to obtain targeted performance curves for select applications.[7−9] Therefore, it is highly desirable to engineer DMFC catalysts and electrode structures that utilize significantly lower $Pt_{1-x}Ru_x$ loadings and maintain current densities in the desired range. There have been attempts to engineer ultralow Pt and $Pt_{1-x}Ru_x$ content DMFC anode catalysts.[7,10,11] These reports have shown mass activity gains as compared to commercially available methanol oxidation catalyst for a Pt-nanoparticle-decorated Ru-black system[7] as well as a number of $Pt_{1-x}Ru_x$-based core–shell type[10,11] catalyst materials. Nonetheless, present DMFC anode catalysts still do not satisfy the activity and durability requirements needed for diverse commercialization of DMFC energy conversion devices. Therefore, new synthesis routes to fabricate active and durable highly dispersed $Pt_{1-x}Ru_x$ nanoparticle DMFC catalysts are desired.

Currently, $Pt_{1-x}Ru_x$ catalysts are prepared by a variety of methods including but not limited to magnetron sputtering, electrochemical deposition, colloidal synthesis, and microemulsion.[1] Unlike most common techniques, sputtering provides a dry fabrication method for surface modification of the support with active metal, and requires no postfabrication processing. This dry technique could greatly speed up fabrication time by eliminating the need for drying and purification steps and also eliminates the use of toxic or flammable materials. Previous $Pt_{1-x}Ru_x$ catalyst materials synthesized via magnetron sputtering were typically deposited via reactive cosputtering from individual Pt and Ru metallic targets to achieve the alloy composition and phase of choice.[4,12−15] Here, we report on the unexpected composition of $Pt_{1-x}Ru_x$ films sputtered from a single $Pt_{0.5}Ru_{0.5}$ alloy target and the improved performance as compared to both cosputtering and solution-based metal-depostition processes.

In this work, we report on the effects of sputtering deposition conditions from an alloyed target on catalyst composition, where we observe an enrichment of Ru, in direct contrast to results previously observed,[16,17] and changes in structure. We further analyze the electrochemical effectiveness of the carbon-supported catalysts as methanol oxidation reaction catalyst materials

Received: April 28, 2011
Revised: July 29, 2011
Published: August 15, 2011

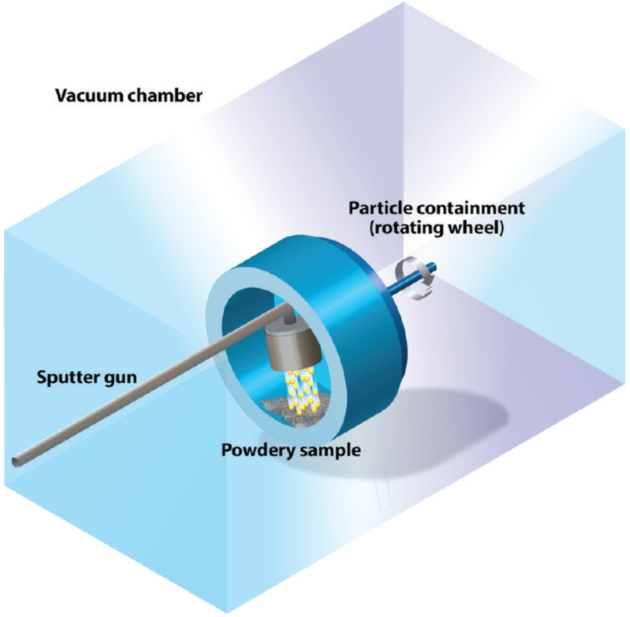

Figure 1. Illustration of custom vacuum instrumentation used to fabricate powder catalysts.

for DMFC, to elucidate key deposition variable-property relationships for these materials. The net result was a 68% increase in specific activity at DMFC operating voltage of 400 mV vs RHE compared to a commercial catalyst of equivalent composition.

EXPERIMENTAL METHODS

Thin Films. $Pt_{1-x}Ru_x$ thin films were sputtered onto Si (100) wafers with a native oxide layer from a single $Pt_{0.5}Ru_{0.5}$ (Plasmaterials) alloyed target with a 2″ Onyx magnetron sputter gun (Angstrom Sciences). The samples were positioned at a distance of 1.5″ directly above the target, and a base pressure below 4×10^{-6} Torr was established prior to deposition in an inert Ar environment. Sputtering was performed using direct current (DC) magnetron sputtering, and radio frequency (RF) magnetron sputtering at various powers and pressures. DC sputtering was performed using a MDX 1.5 kW DC power supply (Advanced Energy, Fort Collins, CO). RF sputtering was performed using a RFX 600 W 13.6 MHz power supply and matching network (Advanced Energy, Fort Collins, CO).

Prior to preparing the initial samples, the target was burned-in for several hours. For each change in sputtering conditions the target was allowed to burn-in and equilibrate for between 5 and 30 min (longer for lower powers). Samples were not fabricated to be equivalent thicknesses but all films were fabricated to be sufficiently thick to be considered bulk films (between 50 and 300 nm).

Oxide thin films were fabricated by adding O_2 to the Ar sputtering gas. The desired mol % of O_2 was achieved by varying the ratio of O_2:Ar, while keeping the deposition pressure constant.

Powder Samples. Powder catalyst samples were fabricated in a custom sputter chamber, similar to the previously reported polygonal barrel-sputtering design.[18−20] An illustration of the basic components of the sputter chamber is given in Figure 1. The chamber, consisting of UHV vacuum components and backed by a 520 L/s turbo molecular pump (Balzers TMP 520, Pfeiffer Vacuum GmbH, Asslar, Germany), housed a powder sample holder ("wheel") mounted on a rotating feedthrough connected to a DC gearmotor (Leeson Electric Corporation, Graphton, WI), and an orthogonally oriented 2″ sputter gun (Onyx Mag 2, Angstrom Sciences, Duquesne, PA). The sputter gun was mounted so the entire sputter assembly sits completely within the wheel, and is pointed toward the powder sample with a sample to target distance of 2.6″. During deposition, the wheel was rotated around the axis of the sputter gun, so the powder sample freely falls down the wall of the wheel, creating a constantly agitated powder sample. During target burn-in the wheel was held in a fixed position with the powder moved behind a small shutter in the wheel.

To facilitate sample transfer, the sputter gun, which was mounted on a compression fitting feed-through, could be retracted from the wheel and the wheel could be completely removed from the sputter chamber.

Sputter gases were introduced from the top through a mass flow controlled gas manifold and were evacuated from the bottom of the chamber. A large area paper filter, changed after each experiment (Whatman #1), served as an effective means to protect the turbo pump from stray particulate ejected from the sample holder.

During a typical experiment, a standard mass (500 mg) of commercially available carbon powder (Cabbot Vulcan XCR72R) was put into a rotating sample holder (rotating wheel), and the chamber was evacuated to less than 5×10^{-6} Torr (typically a few hours, because of limited conductance through the filter paper). Similar to the flat samples, sputtering was performed at 8−10 mTorr with DC powers ranging from 20 to 45 W with a wheel rotation of 30 rpm. The resulting mass loading was controlled by the time the powder was exposed and the sputter power. Similar to the flat substrates, oxidized samples were fabricated by adding oxygen to the sputter gases. Slightly reduced samples were made similarly by adding forming gas (4 mol % H_2:Ar). Fully reduced samples were made by external annealing where the samples were initially heated in a tube furnace to 130 °C in 75 sccm He at 500 Torr for 8 h, then reduced at 270 °C in 50 sccm ultrahigh purity H_2 gas at 500 Torr for 2 h, and then cooled under the H_2 atmosphere.

Chemical and Structural Characterization. The sample composition and structure(s) were measured by X-ray fluorescence (XRF) and X-ray diffraction (XRD) measurements, respectively. A maXXi 5/PIN (Roentgen Analytic) with tungsten target was used for the XRF analysis. The XRF composition was obtained by comparison to a calibrated $Pt_{1-x}Ru_x$ standard using software provided by the XRF manufacturer. A Rigaku Ultima IV with a Cu K-α source and scintillation detector was used for XRD analysis of the powder samples. For $Pt_{1-x}Ru_x$ materials showing a single fcc phase, lattice parameters were obtained by fitting the (111), (200), (220), and (311) Bragg peaks to pseudo-Voigt functions and the extrapolation to $\theta = 90°$ regression method.[21] Crystallite size was obtained by the broadening of the same Bragg peaks using the Scherrer equation after correcting instrument broadening using a LaB6 particle size standard.

Thermogravimetric analysis (TGA) experiments were performed using a TA Q600 (TA Instruments, New Castle, DE) under 100 mL/min of "air" (80% N_2, 20%O_2). Samples were heated to 850 °C at heating rate of 5 °C/min. The metal content was calculated by correlating the XRF composition of the initial catalyst with the final mass residue. For the calculation we assume that the initial mass is metallic in nature and that the final mass at 850 °C is attributed only to RuO_2 and Pt.

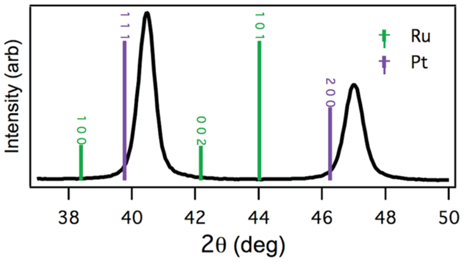

Figure 2. XRD pattern of the alloyed $Pt_{0.5}Ru_{0.5}$ sputter target.

Visual inspection of the powder samples was provided by transmission electron microscopy using a Philips CM200 Transmission Electron Microscope (TEM) with Princeton Gamma-Tech Prism Energy Dispersive X-ray Spectrometer.

Electrochemical Characterization. The powder samples were evaluated for electrochemical performance by rotating disk electrode (RDE) cyclic voltammetry (CV), CO stripping voltammetry, and methanol oxidation reaction (MOR) voltammetry. To fabricate the catalyst modified RDE, 1 mg/mL solutions of catalyst inks were prepared by measuring 10 mg of the catalyst powder, 7.96 mL of water, 2 mL of 2-propanol (IPA), and 40 μL of 5 wt % Nafion solution. These mixtures were bath sonicated for 20 min. Ten microliters of the ink solution were then applied to the glassy carbon RDE.

All electrochemical measurements were conducted at room temperature in a standard three-electrode configuration that utilized a saturated calomel reference electrode and a Pt mesh counter electrode, while the $Pt_{1-x}Ru_x$-catalyzed carbon sample served as the working electrode. All potentials herein have been corrected to the RHE scale. Prior to performing CO stripping voltammetry, the working electrode was "activated" or "cleaned" in a solution of 1 M H_2SO_4 by cycling 50 times from 0.05 to 0.8 V versus RHE. Then neat CO gas was bubbled into 1 M H_2SO_4 for 10 min while the working electrode was held at 0.1 V versus RHE. While the working electrode was still held at 0.1 V versus RHE, neat N_2 was bubbled for 10 min to purge excess CO from the electrolyte. The potential was then swept to 0.8 V versus RHE at 20 mV/s to strip the CO from the surface of the working electrode. Two subsequent sweeps from 0.05 to 1.0 V were then performed to ensure that all the bulk CO had indeed been removed from the electrolyte.

To determine the MOR kinetics, CV measurements were performed in a N_2-purged mixture of 1 M methanol and 1 M H_2SO_4. The potential was swept from 0.3 V versus RHE to 0.8 V versus RHE at 10 mV/s.

■ RESULTS AND DISCUSSION

Initial investigations with X-ray diffraction (XRD) analysis confirmed the sputtering target was an alloyed $Pt_{0.5}Ru_{0.5}$ target (Figure 2). No distinct peaks corresponding to pure segregated Pt or Ru phases were observed in the XRD pattern and the two peaks present were shifted to higher 2θ relative to the Pt (111) and (200) peak positions, indicating an alloyed $Pt_{1-x}Ru_x$ fcc structure.[22,23] Analysis of the target (even after use) showed no evidence of phase segregation.

Thin film samples were sputtered from the alloyed target onto Si wafers with a native oxide at varying powers and pressures using both RF and DC power sources. The alloyed target was conditioned prior to sample fabrication for every new pressure and power condition. The compositions of the thin film samples, as determined by XRF, are shown in Figure 3. XRF, which is insensitive to the phase or bonding of the elements, provides an overall composition independent of structure or phase segregation. Each data point in Figure 3, represents a separate sample that was fabricated using a fixed 1.5″ sample to target distance. In all cases, Ru makes up the remaining composition (not shown) resulting in $Pt_{1-x}Ru_x$ thin films. All the sputtered samples in Figure 3 were measured as Ru rich. Furthermore, for both RF (red triangles) and DC (black squares) sputtering, there is a clear compositional trend with increasing power and the greatest variation in composition observed at the lowest powers. For the DC sputtered films, the Pt composition decreases with increasing power, while the Pt percentage increases for the RF sputtered films. However, both reach an asymptote around $Pt_{0.43}Ru_{0.57}$ at powers above 20 W. At higher powers fewer compositional differences were observed, but no sample reached the equilibrium composition value of the target. Through alteration of the sputtering conditions, the different compositions were reproducibly created independent of the target history or whether RF or DC sputtering was implemented. Samples fabricated with the target moved to a distance of 3″ (twice the distance from the substrates) followed a similar trend and within error gave the same compositions as the samples sputtered from a closer distance, thus eliminating resputtering off the substrate surface as a possible explanation for the compositional trends.

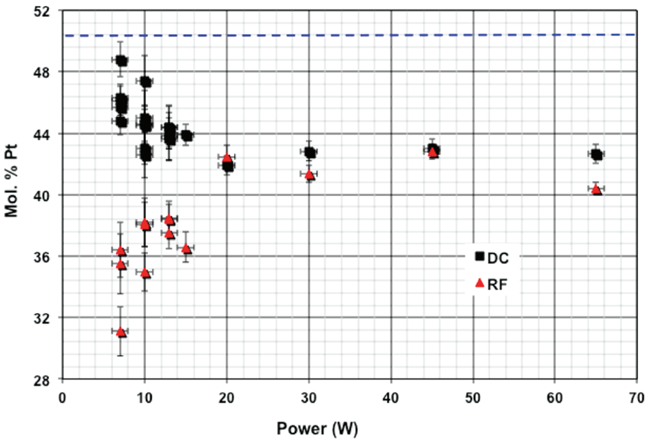

Figure 3. Compositional trends of sputtered thin films as a function of sputter power for both DC and RF sputtered samples.

These results are in direct opposition to previous reports where compositional variations with increasing sputter power were observed for other types of alloyed targets.[16,17] In these reports, the different sputter yields of the individual alloy components results in nonequivalent sputtering rates. Generally, this sputter rate equilibrium occurs on the order of seconds after the plasma is ignited.[17] In our case since the estimated sputter yields for Ru and Pt are very similar,[24] at the ionization energies used, it was expected that the compositions of the thin films should be close to that of the target composition or slightly Pt rich. It has also been shown that sputtering from a mixed target results in different film compositions as a function of power because the composition of the target is constantly in flux; therefore a new target equilibrium has to be re-established for every new deposition condition. This equilibrium generally occurs on the order of minutes to hours dependent on the metals' composition and deposition history.[16,17]

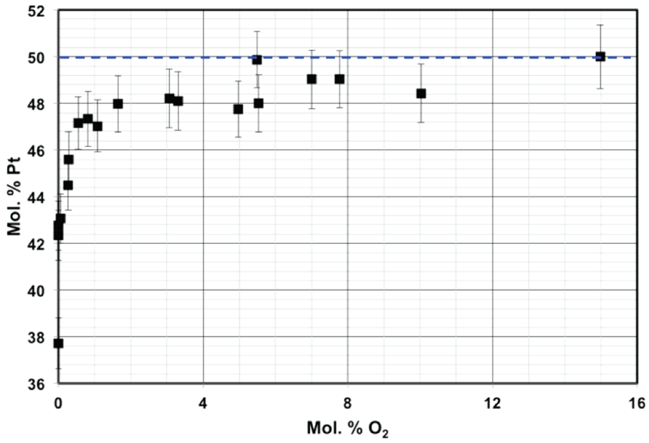

Figure 4. Molar percentage of Pt in sputtered samples as a function of molar percentage O_2 added to sputter gases. All samples were sputtered at 30W DC with the exception of the sample at 0% O_2 which was sputtered at 30W RF in a glovebox sputter system (shown for reference).

To verify that the sputtered thin films were deposited after the target had reached an equilibrium state, thin films were fabricated sequentially under the same conditions using a 10 W DC, 21 mTorr, and 20 min for power, pressure, and deposition time, respectively. The first sample was started after only 3 min burn-in, and the last sample was started 5.5 h later with several samples and continuous sputtering in between. Compositional analysis of the resulting thin films determined that within the error of the measurement the samples were equivalent with a Pt concentration of 36 ± 1.5 mol %, indicating that at these conditions the reaction equilibrium either occurs rapidly or extremely slowly. Depositions in multiple vacuum systems have resulted in correlating thin-film compositions. This reproducibility of thin-film composition for each power independent of previous conditions indicates the reaction equilibrium is fast. However, despite a rapid reaction equilibrium time, the samples do not reflect the composition of the target, indicating an extremely slow target equilibrium time or disparate sputter yields.

Alternatively, when the experiments were repeated in a sputter chamber that opens to an inert atmosphere glovebox, reducing the presence of adsorbed O_2 and H_2O on the interior of the sputter chamber, the molar percentage of Pt in the resulting thin films unexpectedly dropped further. Samples fabricated at 10 W RF and 30 W RF resulted in thin film compositions of 30.2 ± 1.7 mol % Pt and 37.7± 1.1 mol % Pt, respectively. Samples prepared using forming gas (4 mol % H_2/Ar) resulted in samples that were slightly more Ru rich than samples prepared using only Ar, but not as Pt depleted as the inert environment samples. Samples prepared at 21 mTorr, using 20 W DC and 45 W DC resulted in $Pt_{0.42}Ru_{0.58}$ and $Pt_{0.41}Ru_{0.59}$ compositions, respectively. Subsequent experiments were performed where the O_2 molar concentration was changed by modifying the Ar/O_2 sputter gas ratio while keeping the deposition pressure constant at 21 mTorr. As demonstrated in Figure 4, the Pt concentration of the samples increased with the added O_2 gas concentration until the Pt/Ru ratio matched that of the target; above about 5 mol % O_2 in the sputter gas.

With copious amounts of oxygen, RuO_2 and PtO_2 formed on both the target and the sample surface. In this situation, the samples reflect the composition of the target, as found by XRD. The existence of oxides of *both* species results in the restoration of the target equilibrium and the Pt and Ru atoms sputter at similar rates. The most likely explanation for the observed compositional trends at low oxygen concentrations is preferential oxide formation[25,26] and a difference in sticking coefficients of the Ru and Pt atoms. These results suggest that the Ru atoms are much more likely to stick than the Pt atoms. From heat of formations, RuO_2 is more likely to form than PtO_2 with limited oxygen presence. Possibly the oxygen in the system preferentially forms RuO_2, hence driving the target equilibrium. The oxygen forms RuO_2 on the target surface, causing more Ru to move from the underlying target to compensate and increasing the sputter yield of Ru. With the addition of more oxygen, the RuO_2 formation competes with the sputter yield decreasing the amount of Ru, that is, effectively increasing the relative Pt concentration, reaching the samples surface. Once enough oxygen is present to form both PtO_2 and RuO_2 as fast as the atoms reach the target surface, the target equilibrium is restored.

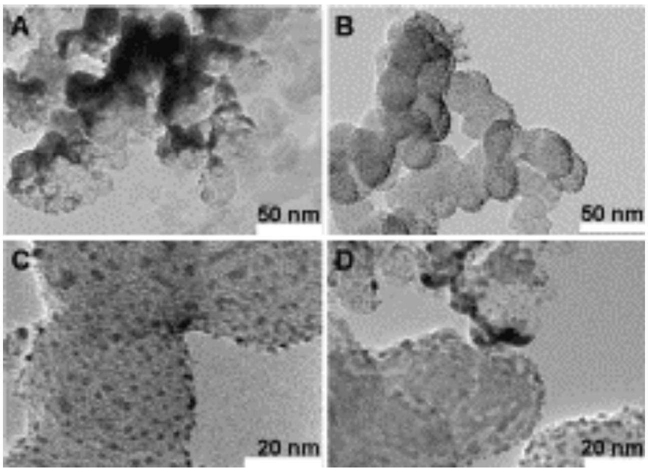

Figure 5. TEM images of typical sputtered catalyst materials. Sample information given in Table 1. (A) Representative image (Sample H) showing heterogeneous deposition from line-of-sight sputtering. Regions of high metal aggregation juxtapose regions of disperse discrete nanoparticles. (B) A region of evenly dispersed and homogeneous nanoparticles scattered on all sides of the carbon support. Sample J shown. (C, D) Different regions of Sample B. The more spherical and isolated nanoparticles are more typical (C), but regions where the nanoparticles grow together to form networks (D) are common, especially for post-annealed samples.

To demonstrate the applicability of fabricating high-surface area catalyst materials onto inexpensive and lightweight carbon supports by these methods, sputtered powder samples were fabricated in the custom sputter chamber described earlier. This platform resulted in a much higher surface area, increasing the signal-to-noise ratio for both electrochemical and structural analysis. Similar compositional trends that were dependent on the conditions used for sputtering were observed for these powder samples. However, without significant effort to degas the powders, the compositional window was smaller and was shifted toward higher platinum loading. Except for highly oxidizing conditions the compositions remain Ru rich.

Figure 5 shows TEM images of several catalyst samples. These images represent the typical results of this type of deposition with similarities to previous reports of sputtered catalysts that were prepared by cosputtering methods.[12,19,20] Given the line-of-sight nature of sputtering, some shadowing was expected. Despite macroscopic heterogeneous deposition, the sputtered $Pt_{1-x}Ru_x$

Table 1. Summary of Composition, Weight Percent, and Structural and Electrochemical Parameters for Samples Fabricated with Different Sputtering Conditions[a]

sample name	deposition description	XRF composition ratio Pt:Ru	TGA weight percent	XRD lattice constant Å	XRD particle size Å	electrochemical surface area m^2/g metal	MOR current density @ 400 mV uA/cm^2 metal	MOR current density @ peak uA/cm^2 metal	voltage @ peak mV
A	45 W DC; 10 mol % O_2:Ar; 60 min	47: 53	26.3	3.877 ± 0.006	44 ± 2	57.0	13	98	763
B	45 W DC; 10 mol % O_2:Ar; 60 min post reduced	48:52	39.0	3.870 ± 0.001	36 ± 2	28.0	2	100	758
C	45 W DC; 4 mol % H_2:Ar; 60 min	45:55	33.1	3.86 ± 0.04	45 ± 2	51.4	6	83	720
D	45 W DC; 4 mol % H_2:Ar; 60 min; post reduced	46:54	30.4	3.86 ± 0.03	41 ± 2	49.3	4	118	708
E	45 W DC; 100 mol % Ar; 60 min; post reduced	46:54	26.8	3.860 ± 0.004	42 ± 2	54.1	6	95	709
F	45 W DC; 100 mol % Ar; 60 min	47:53	27.4	3.860 ± 0.004	41 ± 2	29.2	1	46	734
G	15 W DC; 10 mol % O_2:Ar; 300 min	48:52	37.2	N/A	N/A	40.3	1	48	744
H	45 W DC; 20 mol % O_2:Ar; 60 min; 45 W DC; 10 mol % O_2:Ar; 60 min	49:51	42.0	3.85 ± 0.04	27 ± 1	41.9	31	190	754
I	45 W DC; 50 mol % O_2:Ar; 120 min	49:51	48.6	N/A	N/A	29.6	11	144	781
J	45WDC; 10 mol % O_2:Ar; 25 mTorr; 60 min	52:48	29.2	N/A	N/A	73.0	32.1	207	765
JM10000	commercial catalyst	50:50	59.5	3.88 ± 0.03	31 ± 1	50−60	19	246	708
JM5000	commercial catalyst	50:50	30.0	3.87 ± 0.02	24 ± 2	69	29	220	746
Target	$Pt_{0.5}Ru_{0.5}$ alloyed target	50:50	N/A	3.895 ± 0.004	N/A	N/A	N/A	N/A	N/A

[a] A commercial catalyst standard (JM10000 = Johnson Matthey HiSpec 10000, JM5000 = Johnson Matthey HiSpec 5000, Alfa Aesar, Ward Hill, MA) and the sputtering target used are given for reference.

results in nanoparticles decorating the carbon surface throughout the carbon matrix (Figure 5B). Visual inspection shows that the deposition is defined by regions of high coverage and metal particle agglomeration (Figure 5D), mixed with regions of sparsely populated but discrete nanoparticles, and regions of highly populated discrete nanoparticles (Figure 5C). All of these regions were observed in most of the catalysts. Catalysts that were post-annealed were prone to more regions with aggregated particles, but still had high densities of discrete particles.

Several samples with varied deposition parameters were fabricated to understand the effects of the deposition conditions on the physical and electrochemical properties of the fabricated catalysts. A summary including metal composition and metal loading of the resulting materials is given in Table 1. The parameters varied were deposition gas composition and concentration, sputtering power and sputtering pressure, which combined, composed a complex matrix with specific structural and electrochemical properties.

XRD patterns of the samples in Table 1 are shown in Figure 6 (refer to Table 1 for full description of each sample shown in the figure). Each panel in Figure 6 compares the effects of varying one sputtering parameter while the rest of the deposition process conditions are held constant. Figure 6A and 6B compare the effects of the gas composition and concentration, and Figure 6C and 6D compare the effects of the sputtering power and sputtering pressure, respectively.

In the bulk, platinum and ruthenium alloy form a solid solution with an fcc structure for compositions up to 62 mol % Ru. For thin $Pt_{1-x}Ru_x$ films, the solid solution onset occurs near ~30 mol % Ru.[13] All the samples deposited in this study resulted in alloyed $Pt_{1-x}Ru_x$ structures with no mixed or hcp Ru phase observed. For the sputtering conditions used in Figure 6A (45W DC, 8 mTorr, 60 min), the gas compositions had only small effects on the structure. All three samples exhibited the same crystalline peaks. The samples sputtered in 4 mol % H_2:Ar and in pure Ar resulted in identical structures and similar compositions with only noticeable difference between these samples is the rate of deposition. The samples sputtered using forming gas always resulted in slightly higher metal loadings. Comparison of oxidizing sputter conditions versus reducing sputter conditions elucidates subtle shifts in the peak positions (see inset), presumably because of small changes in composition (similar to those observed in Figure 3). The more oxidizing conditions shifted the alloyed peaks toward the pure Pt peak positions and the reducing conditions shifted the peaks away from the Pt peaks. Peak position differences between the Ar and 4 mol % H_2:Ar were not observable above the background.

Sample A XRD data (red data in Figure 6A, C, and D) has slightly broader peaks and an elevated background compared to the other XRD data. When samples were made with higher O_2 concentrations, but the same sputtering conditions (shown in

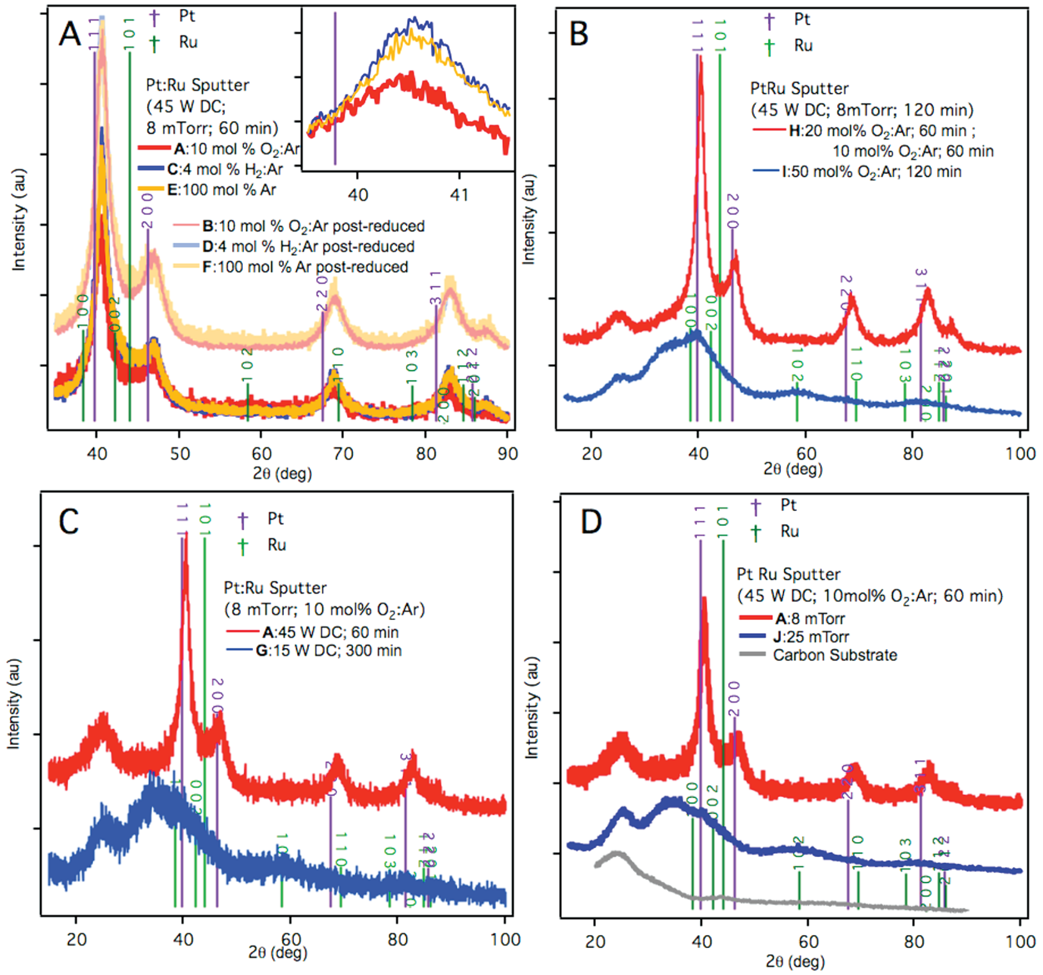

Figure 6. XRD patterns of samples fabricated with various sputtering conditions. For each panel one variable is compared while the rest are left constant. See Table 1 for a complete description of each sample. (A) The effects of sputter gas type. (B) The effects of sputter gas concentration. (C) The effects of sputter power. (D) The effects of sputter pressure.

Figure 6B), the apparent crystalline nature of the samples decreased. This change in crystallinity may be due to diminished order (amorphous tendencies) or a reduction in the size of the particles. However, the TEM studies indicate no significant change in the average particle size. A post-annealing treatment in a reducing environment was used to return the samples to a crystalline state with a significant increase in features associated with long-range atomic order. Except for the oxidized samples, no difference was observed structurally between the as-produced and the postreduced samples (see Figure 6A). However, this annealing technique was a successful means to generate crystalline samples with bulk 50:50 molar compositions, as measured by XRF.

The observed structural changes can be reproduced by tuning the speed of deposition (see Figure 6C). **Sample A** (red data in Figure 6A, **C** and **D**) and **Sample G** (blue data in Figure 6C) were fabricated with the same gas compositions but at different sputtering powers. The faster deposition (higher power) resulted in a more crystalline structure. If instead the sputtering power was left constant and the sputtering pressure was changed, shown in Figure 6D, the crystalline peaks associated with the metal phases decreased. These observations indicate that the resulting structure, either amorphous or crystalline, results because of a precise balance of oxygen concentration with metal flux.

Despite the structural variations in the samples, the resulting lattice constants and the estimated particles' sizes remained similar. Note that the lattice constant and particle size estimation calculations require a crystalline phase, therefore these estimations are not feasible for samples lacking appreciable long-range order. These calculated variables are an average of the whole sample (including any agglomerates), but correlate with the visual analysis provided by TEM. Visually, excluding aggregate areas, all the samples resulted in nanoparticles with an average size of 3.5 nm ±0.5 nm. These parameters are similar to the best performing commercially available catalyst materials.

To assess the influence of the sputtering conditions on the electrochemical performance, the active surface area and the catalyst activity of each sample were measured by CO stripping voltammetry and MOR CV measurements, respectively. These data are shown in Figure 7, and specific comparison points are given in Table 1. In each case, the MOR is corrected to the measured electrochemical $Pt_{1-x}Ru_x$ surface area; however, a comparison of the measured surface area is given relative to the catalyst metal loading in Table 1. Comparing the overall peak current and position as well as the onset potential, the MOR experiments were used to evaluate how the deposition-induced properties of the catalysts influenced their methanol oxidation performance relative to other fabricated materials and relative to

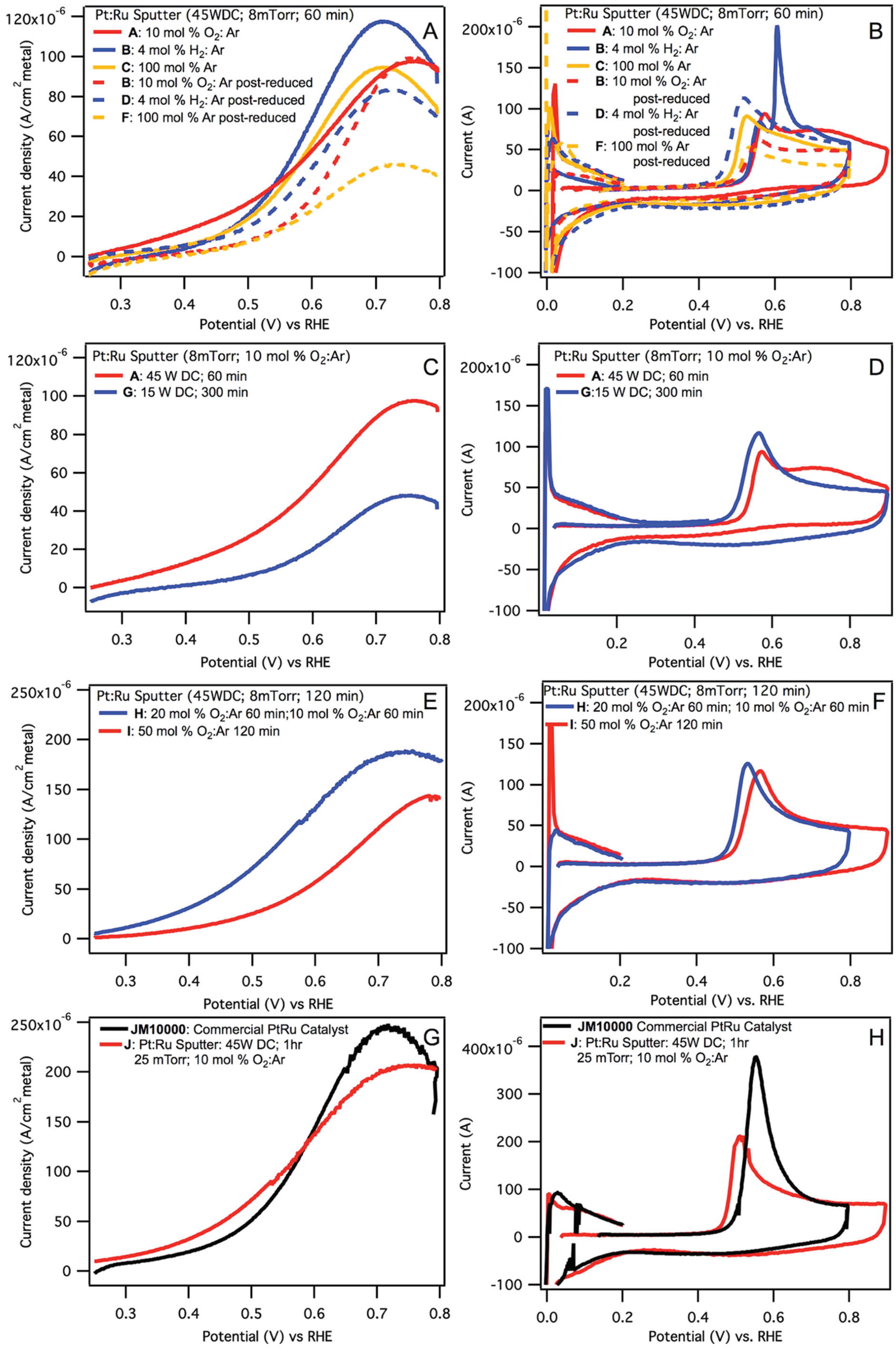

Figure 7. Electrochemical performance of the sputtered catalyst samples. A, C, E, and G show current density as a function of potential for methanol oxidation reaction analysis. B, D, F, and H show the current versus potential for CO stripping analysis used to determine surface area. A and B show the effects of deposition gas composition and post-annealing. C and D show the effects of sputter power. E and F show the effects of O_2 concentration. G and H compare the best performing catalyst to a commercial standard.

commercial standards. These data are shown in Figures 7A, 7C, 7E, and 7G. CO stripping experiments were used to determine the electrochemical surface area and to infer the efficiency of complete oxidation of intermediate methanol reaction products such as, CO. For example, an efficient methanol oxidation catalyst should also show good CO oxidation performance. In this case the CO stripping "kick-off" and peak potentials should be shifted to more negative values as compared to a less efficient catalyst material. The utilization of Ru is key when engineering an efficient methanol oxidation catalyst. Ru surface species, such as Ru_xO_y and RuOH, have been speculated to facilitate the complete oxidation of CO to CO_2. Further, particle size effects also influence these reaction processes. Figures 7B, 7D, 7F, and 7H show the CO stripping curves for the sputtered Pt−Ru materials. The trends with deposition parameters observed in the CO stripping curves do not directly correlate with any of the *bulk* structural observations. Without precise knowledge of the composition and state of the surface (top few atomic layers) it is difficult to establish structure-to-property correlations and ascribe meaningful physical interpretations. Further complications arise because of the bifunctional nature of catalysts materials that support reaction processes where active intermediates are formed, such as in the oxidation of methanol. As a result, the overall methanol oxidation performance is influenced by the proximity of the active sites on the catalyst surface. Therefore, the CO stripping curves serve as an indication of active surface area and overall relative improved performance.

Figure 7A and 7B show the effect of the sputtering gas composition on the catalyst performance. The gas composition has minimal effect on the resulting active surface area, and the MOR peak currents are all very similar. However both the peak position and the onset potential are influenced by the sputter gas composition. The most negative MOR onset potentials were always observed for samples fabricated in an oxygen-rich environment. There are two possible explanations for this result: (1) that an oxidizing agent, in this case O_2 gas, is needed to form the active Pt and/or Ru phases for the MOR. It has been speculated that Ru-oxide surface species contribute to the conversion of intermediate reaction products that are formed during the MOR process, specifically CO.[1,27] (2) Alternatively, metal oxide species that form allow for subsequent deposition and (or otherwise contribute to) formation of the active $Pt_{1-x}Ru_x$ phase. In this case the oxide phase is a prerequisite to creation of the desired $Pt_{1-x}Ru_x$ surface phase.

The oxidized samples also resulted in higher MOR peak potentials (by ~50 mV). This shift is likely the result of small differences in relative Pt:Ru concentration (the oxidized samples had on average 3−4% higher Pt concentration) which also causes a shift in the relative peak position in the CO stripping curves. Interestingly, the postreduced sample peak potentials remained the same, but the peak currents were always reduced and the onset potentials were always shifted to higher potential compared to the unreduced versions. These results correlate to a measured reduction in electrochemical surface area, but are not reflected in any of the structural investigations or significant changes in particle size.

Increases in metal loading and O_2 concentration during sputtering, shown in Figure 7C, 7D, 7E and 7F improved the performance (across all metrics) of the catalyst materials. However, it was observed that altering any one deposition parameter resulted in multiple structural and electrochemical property changes, so that reoptimization of the other parameter space was required, that is, most of the parameters are interdependent. We were able to ascertain that the ideal O_2 concentration appears to be between 10 mol % and 20 mol % (Figure 7E and 7F).

Finally, the effect of deposition pressure is shown in Figure 7G and 7H. This sample (**Sample J**), performs better than the commercial catalyst material in the kinetic region, and also exhibited similar peak currents. At least in part, this result is explained by an increase in active surface area afforded by sputtering at higher pressure (Note that the axis in Figure 7H is twice as large as the other CO stripping figures). Comparing the CO stripping performance of **Sample J** to the commercial standard, shown in Figure 7H, indicates that further improvements need to be made to the surface area of the sputtered catalyst. However, the metal weight loading of the sputtered catalyst is half that of the commercial standard. The sample that performed the best electrochemically (**Sample J**) was sputtered in 10 mol % O_2:Ar at 25 mTorr using 45W DC for 60 min. These parameters resulted in a considerable improvement in the kinetic region and comparable peak performance relative to JM1000. This sample also had a ~40% increase in electrochemical surface area despite half the metal loading. Using cosputtering methods, Inoue et al. were also able to synthesize commercially competitive catalyst materials.[18−20] In these studies, they were able to produce both alloyed and phases separated particles, but their synthesized alloyed $Pt_{0.50}Ru_{0.50}$ performed as well as commercial catalysts despite 1/10th of the metal loading. Together with the present work, these studies demonstrate the applicability of these sputtering techniques to high surface area catalyst materials.

CONCLUSIONS

In the sputtering of Pt−Ru alloyed catalysts from a single composition target the best performing catalysts are fabricated in an oxygen rich environment at high power and high pressure. The trends of the effects of the deposition conditions on both the structure and the electrochemical performance are clear. However, structure−property relationships correlating the catalyst's structure to its electrochemical performance still remain elusive. Samples both with and without long-range crystalline order that were fabricated using completely different deposition parameters behave similarly electrochemically, while samples that have similar bulk structure are electrochemically polarized. It is expected that optimizing the process parameters can make further improvements to MOR performance. Additionally, because the performance seemingly depends on the junction of multiple variables, it may be possible that there is more than one route to manufacture the best catalyst by this method. Further experiments are required targeting the surface composition and surface structure to determine the structure-electrochemical relationships.

Using a unique sputtering method we have demonstrated a dry processing technique to fabricate commercially competitive, low-metal-loading $Pt_{1-x}Ru_x$ catalyst materials for DMFC anodes. $Pt_{1-x}Ru_x$ metal nanoparticles of varying composition were sputtered from a single alloyed target to decorate the surface of a carbon matrix support. Adjusting the individual sputtering parameters provides distinctive yet reproducible chemical, structural, and electrochemical properties. Optimizing these sputter methods will produce catalyst materials that surpass existing performance levels of methanol oxidation by commercial catalysts in terms of oxidation efficiency and durability. Optimization should include deposition gas concentration and pressure along with the exact metal loading needed to maximize methanol oxidation and to make the optimal membrane electrode assembly for DMFC. It may also be possible to treat the carbon surface prior to sputtering to create and stabilize nucleation sites for nanoparticle deposition to also increase performance and durability.

AUTHOR INFORMATION

Corresponding Author

*E-mail: arrelaine.dameron@nrel.gov. Phone: 303-384-7838. Fax: 303-384-6490.

Funding Sources

This work was supported by the U.S. Department of Energy under Contract No. DE-AC36-08-GO28308 with the National Renewable Energy Laboratory and the Army Research Office under Grant W911NF-09-1-0528.

■ ACKNOWLEDGMENT

The authors thank Raymond David for Visual Design contributions and Dane Gillaspie and Joshua Martin for their help with the sputtering experiments.

■ REFERENCES

(1) Liu, H. S.; Song, C. J.; Zhang, L.; Zhang, J. J.; Wang, H. J.; Wilkinson, D. P. *J. Power Sources* **2006**, *155*, 95.

(2) Zhao, T. S.; Xu, C.; Chen, R.; Yang, W. W. *Prog. Energy Combust. Sci.* **2009**, *35*, 275.

(3) Kua, J.; Goddard, W. A. *J. Am. Chem. Soc.* **1999**, *121*, 10928.

(4) Strasser, P.; Fan, Q.; Devenney, M.; Weinberg, W. H.; Liu, P.; Norskov, J. K. *J. Phys. Chem. B* **2003**, *107*, 11013.

(5) Bock, C.; MacDougall, B.; LePage, Y. *J. Electrochem. Soc.* **2004**, *151*, A1269.

(6) Dinh, H. N.; Ren, X.; Garzon, F.; Zelenay, P.; Gottesfeld, S. *J. Electroanal. Chem.* **2000**, *491*, 222.

(7) Arico, A. S.; Baglio, V.; Modica, E.; Di Blasi, A.; Antonucci, V. *Electrochem. Commun.* **2004**, *6*, 164.

(8) Ren, X. M.; Wilson, M. S.; Gottesfeld, S. *J. Electrochem. Soc.* **1996**, *143*, L12.

(9) Reshetenko, T. V.; Kim, H. T.; Krewer, U.; Kweon, H. J. *Fuel Cells* **2007**, *7*, 238.

(10) Ando, Y. J.; Sasaki, K.; Adzic, R. *Electrochem. Commun.* **2009**, *11*, 1135.

(11) Sasaki, K.; Adzic, R. R. *J. Electrochem. Soc.* **2008**, *155*, B180.

(12) Caillard, A.; Coutanceau, C.; Brault, P.; Mathias, J.; Leger, J. M. *J. Power Sources* **2006**, *162*, 66.

(13) Kim, T. W.; Park, S. J.; Jones, L. E.; Toney, M. F.; Park, K. W.; Sung, Y. E. *J. Phys. Chem. B* **2005**, *109*, 12845.

(14) Park, K. W.; Ahn, K. S.; Choi, J. H.; Nah, Y. C.; Sung, Y. E. *Appl. Phys. Lett.* **2003**, *82*, 1090.

(15) Warren, A. P.; Todi, R. M.; Yao, B.; Barmak, K.; Sundaram, K. B.; Coffey, K. R. *J. Vac. Sci. Technol., A* **2008**, *26*, 1208.

(16) Ohring, M. *Materials Science of Thin Films*, 2nd ed.; Academic Press: San Diego, 2002.

(17) Westwood, W. D. *Sputter Deposition*; AVS: NewYork, 2003.

(18) Inoue, M.; Akarnaru, S.; Taguchi, A.; Abe, T. *Vacuum* **2008**, *83*, 658.

(19) Inoue, M.; Nishimura, T.; Akamaru, S.; Taguchi, A.; Umeda, M.; Abe, T. *Electrochim. Acta* **2009**, *54*, 4764.

(20) Inoue, M.; Shingen, H.; Kitami, T.; Akamaru, S.; Taguchi, A.; Kawamoto, Y.; Tada, A.; Ohtawa, K.; Ohba, K.; Matsuyama, M.; Watanabe, K.; Tsubone, I.; Abe, T. *J. Phys. Chem. C* **2008**, *112*, 1479.

(21) Cullity, B. D.; Stock, S. R. *Elements of X-ray diffraction*, 3rd ed.; Prentice Hall: New York, 2001.

(22) Vogel, W.; Britz, P.; Bonnemann, H.; Rothe, J.; Hormes, J. *J. Phys. Chem. B* **1997**, *101*, 11029.

(23) Yu, X. Y.; Jiang, Z. Q.; Meng, Y. D. *Plasma Sci. Technol.* **2010**, *12*, 224.

(24) Berg, S.; Katardjiev, I. V. *J. Vac. Science & Technol., A* **1999**, *17*, 1916.

(25) Reuter, K.; Scheffler, M. *Phys. Rev. B* **2002**, *65*.

(26) *CRC Handbook of Chemistry and Physics*; CRC Press: Boca Raton, FL, 2000; Vol. 81.

(27) Chen, W. M.; Xin, Q. *Chem. J. Chin. Univ.* **2009**, *30*, 1259.